J Intell Robot Syst (2010) 57:49–64
DOI 10.1007/s10846-009-9370-6

Vision-based Position Control of a Two-rotor VTOL miniUAV

E. Rondon · S. Salazar · J. Escareno · R. Lozano

Received: 1 February 2009 / Accepted: 1 August 2009 / Published online: 16 September 2009

Abstract In this paper we address the stabilization of the attitude and position of a birotor miniUAV to perform autonomous flight. For this purpose, we have implemented a Kalman-based sensor fusion between inertial sensors (gyros-accelerometers) and the optical flow (OF) provided by the vehicle. This fusion algorithm extracts the translational-OF (TOF) component and discriminates the rotational OF (ROF). The aircraft's position is obtained through an object detection algorithm (centroid tracking). Newton-Euler motion equations were used to deduce the mathematical model of the vehicle. In terms of control we have employed a saturated-based control to stabilize the state of the aircraft around the origin. Experimental autonomous flight was successfully achieved, which validates the sensing strategy as well as the embedded control law.

Keywords Optical flow · Nonlinear control · VTOL aircraft

1 Introduction

The development of mini UAVs and micro UAVs has recently motivated new research areas in different disciplines, such as electronics, mechanics, aeronautics,

E. Rondon (✉) · R. Lozano
Université de Technologie de Compiègne, Heudiasyc, UMR CNRS 6599, Compiègne, France
e-mail: rondoned@hds.utc.fr

R. Lozano
e-mail: rlozano@hds.utc.fr

S. Salazar · J. Escareno
Laboratoire Franco Mexicain d'Informatique et Automatique,
UMI-CNRS 3175, Mexico, DF, Mexico

J. Escareno
e-mail: jescareno@ctrl.cinvestav.mx

automatic control just to mention a few. Such vehicles have great potential for search and rescue missions, homeland security, real-time forest fire monitoring, surveillance of sensitive areas (borders, ports, oil pipelines), remote sensing, etc. Accurate navigation and efficient control of the vehicle are essential to successfully accomplish such missions. Furthermore, small UAVs impose weight and size constraints which exclude the use of heavy sensors. Light sensors are usually less accurate and therefore suitable estimation and control algorithms should be developed, since the performance of the closed loop control system will be as good as the quality of the feedback sensor signal.

Inertial sensors, gyroscopes and accelerometers, provide rotational velocity and linear acceleration respectively. The numerical integration of these signals can provide the attitude, translational position and velocity of the vehicle. These measurements are valid only for a short period of time, since the signal drifts due to inherent noise and bias. Thus, for a reliable attitude measurement, a fusion between accelerometers and gyroscopes is needed. Concerning the position, the GPS is fused with inertial sensors (INS) to provide periodic corrections, in order to obtain a more accurate (drift-less) position measurement. However, the GPS signal is not available for indoor locations or certain urban zones (urban canyon problem). To overcome this location estimation issue, an alternative strategy is the combination of artificial vision with inertial sensors to extract a valid position measurement of the aerial robot.

Previous works have been developed using visual-based sensing estimation.

In [2] a visual control system is presented which aims at maintaining a constant optical flow (OF). The OF is obtained from a camera which is vertically fixed to the platform to avoid the acquisition of OF produced by rotational motion of the flying engine. In [3] the author established a relation between the OF ($\frac{pixel}{s}$) and the actual rotation ($\frac{degrees}{s}$), through the knowledge of the corresponding inter-pixel angle. After a calibration, the cancelation of the rotational components is obtained by substracting the gyroscopic value from the OF measurement. Other approach was proposed in [4], where the rotational optical flow (ROF) is canceled by counter-rotation of the OF sensors. The flying object orientation is then stabilized and the visual system detects pure translational OF (TOF). In [5] the authors developed a methodology to compensate the ROF. Using the angular rate they computed the rotational component for each pixel, where an estimated of the OF has been acquired. The rotational component is then subtracted from the measured OF, and an estimation of the angular velocity is finally obtained. Although this approach seems natural, the noise in the measurements is not taken into account. The fusion of inertial and visual information has been addressed by several authors, for different applications. In [6] an eight-rotor mini UAV employs an optical flow feedback for translational motion damping. This particular design obeys to the idea of enhancing the attitude stability by decoupling the attitude and position control and leading to a fully-actuated dynamics. The pitch and roll angular positions are first stabilized around the origin so that the OF measurement is a good estimate of the translational velocity. In [7] the authors have used inertial sensors to improve the OF measurement for obstacle detection. In [8] a gyroscope sensor is used to decompose rotational and translational motion from the visual scene in order to increase the accuracy of the 3D shape reconstruction. Another technique to extract 3D motion from estimated velocity vectors from a number of points of the image

is the Egomotion [9]. In this method the rotational components are eliminated via algebraic operations and the translational components are estimated using a least squares method. However, the algorithms for such technique are computationally expensive.

Most of small UAVs have underactuated dynamics, i.e. the vehicle's horizontal motion is generated by the pitch and roll angular displacements. Hence, the measured OF is produced by both the translational and the rotational motions. An effective visual-based control of the UAV's position requires the use of inertial sensors (accelerometer and gyroscopes) to eliminate the ROF component. Yet another alternative to measure only the translational motion is to use gyrostabilized cameras. However such cameras are expensive and heavy.

In the present paper we consider a platform composed of a two-rotor mini UAV and two external cameras. An alternative strategy is presented to estimate the translational position and velocity of the mini UAV. The flying engine has an inertial measurement unit (IMU) to measure the orientation. The position and velocity are obtained using two external cameras which provide frontal and lateral views of the vehicle. A Kalman filter is proposed to fuse the visual information with the IMU measurement in order to remove the bias due to ROF, depth and sensors noise. The resulting Kalman filter estimate is incorporated into the control algorithm to stabilize the 6-DOF nonlinear dynamics (attitude and position) of the aerial robot. The proposed control strategy has been successfully tested in the real platform.

The paper is organized as follows: Section 2 describes the sensing system and the fusion algorithm. In Section 3, the dynamical model of the vehicle is obtained. Section 4 presents the saturation-based control algorithm to stabilize the flight dynamics. Section 5 describes the experimental setup and shows the results obtained during the autonomous hover flight of the vehicle.

2 Position and Velocity Estimation

2.1 Inertial Sensors

The output of a gyroscope can be decomposed as follows

$$\omega_o = \omega_i + \delta\omega_b + \delta\omega_{to} + \delta\omega_r \tag{1}$$

where ω_o is the measured gyroscope output, ω_i is the real value, $\delta\omega_b$ is a known constant bias, $\delta\omega_{to}$ is a temperature dependent bias, and $\delta\omega_r$ is a random-walk process.

2.2 Visual Sensors

The goal of our approach is to estimate the position of an aircraft at each image obtained from the two cameras. These cameras are arranged orthogonally, the frontal camera (cam_y) and lateral camera (cam_x) measure the displacement of the vehicle in the $Y^{\mathcal{B}}Z^{\mathcal{B}}$ and $X^{\mathcal{B}}Z^{\mathcal{B}}$ planes respectively (see Figs. 1 and 2).

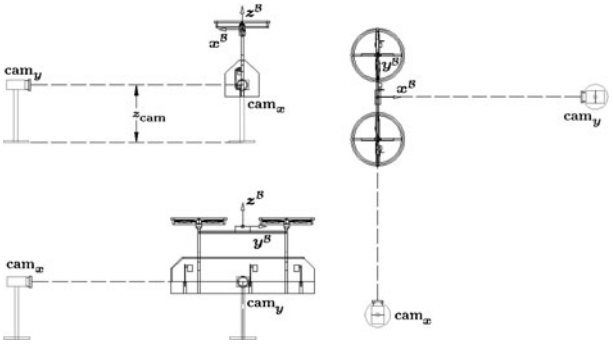

Fig. 1 Visual perspective of the cameras: **a** XZ-plane (*left-top*) **b** YZ-plane (*left-bottom*) **c** XY-plane (*Right*)

2.2.1 Position

In order to increase the contrast in the image of the camera, the fuselage of the aerial robot is covered with points (see Fig. 3). Notice that for each camera, every point on the aircraft surface has a corresponding projected point on the image plane. Hence, the position of the aircraft can be estimated using the centroid or barycenter of these points. In fact the barycenter's position can be expressed as the initial position plus the displacement during the interval $[t, t + \Delta t]$.

$$\begin{aligned} x_{brc}(t + \Delta t) &= x_{brc}(t) + \int_t^{t+\Delta t} V_x dt \\ y_{brc}(t + \Delta t) &= y_{brc}(t) + \int_t^{t+\Delta t} V_y dt \end{aligned} \tag{2}$$

Fig. 2 Experimental setup

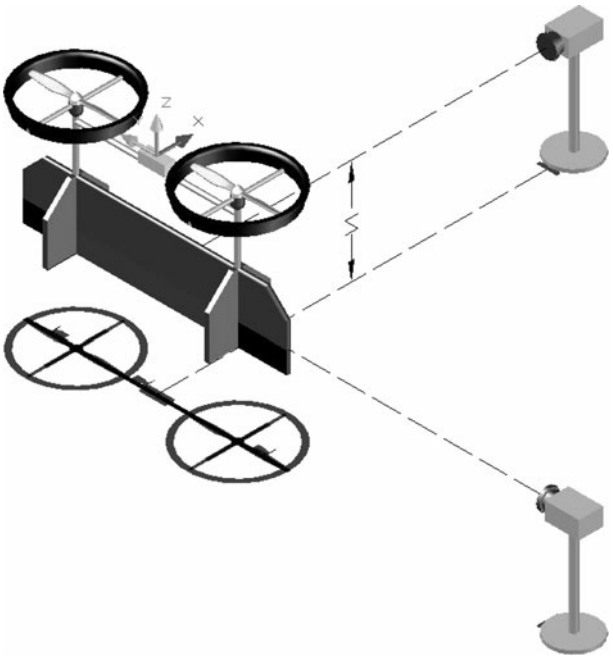

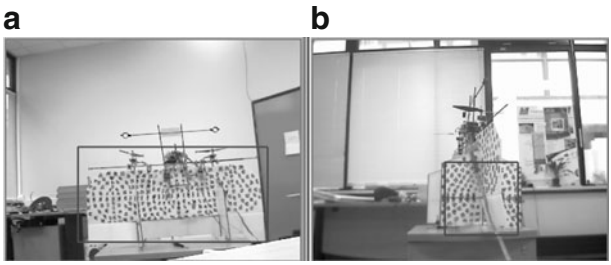

Fig. 3 Visual perspective of the cameras: **a** Frontal camera (*left*) **b** Lateral camera (*right*)

The method used to detect the object was proposed by Viola and Jones [10], this method is a machine learning approach capable of processing images extremely rapidly. The main motivation for using this approach is the high detection rate which makes this algorithm suitable for real time applications. Before implementing the algorithm a learning stage is needed. For this purpose a "training" set of 1000 images of the aircraft body frame were used, as well as 80 images of the surrounding environment. The low number of environment images is justified by the fact that the environment remains fixed. When the environment may change, a larger number of samples of positive (aircraft) and negative (environment) images are needed to render the detector more robust. The samples were chosen so that the detector is robust with respect to (w.r.t.) slight variations of light intensity, cameras parameters and environment.

2.2.2 Optical Flow (OF)

The OF is widely used to compute an approximation of motion field through time-varying image intensity. Among the diverse approaches to compute OF [1], we have implemented the Lucas-Kanade pyramidal algorithm [11] in combination with a texture-detecting algorithm. This method provides an accurate estimation of the motion field. The points are placed on the vehicle's surface with a specific pattern (see Fig. 3) enabling the computation of the OF. The texture detector also neglects the neighborhood, where the motion field cannot be accurately determined.

The point $p(x_i, y_i)$ in the image plane of the camera has a corresponding point $P(X, Y, Z)$ in the real world, which is obtained with a perspective projection of a pinhole camera in the following way:

$$\begin{aligned} x_i &= f\frac{X}{Z} \\ y_i &= f\frac{Y}{Z} \end{aligned} \tag{3}$$

where (x_i, y_i) represents the point in the image plane, f is the focal length of the camera and Z is the distance between the camera and the aircraft. Differentiating both sides of (3) leads us to the familiar equations of OF [12]

$$\begin{bmatrix} OF_{x_i} \\ OF_{y_i} \end{bmatrix} = T_{OF} + R_{OF} \tag{4}$$

with

$$T_{OF} = \frac{1}{Z}\begin{bmatrix} -f & 0 & x_i \\ 0 & -f & y_i \end{bmatrix}\begin{bmatrix} V_{\mathrm{x}} \\ V_{\mathrm{y}} \\ V_{\mathrm{z}} \end{bmatrix} \tag{5}$$

and

$$R_{OF} = \begin{bmatrix} \frac{x_i y_i}{f} & -\left(f + \frac{x_i^2}{f}\right) & y_i \\ \left(f + \frac{y_i^2}{f}\right) & -\frac{x_i y_i}{f} & -x_i \end{bmatrix}\begin{bmatrix} \omega_{\mathrm{x}} \\ \omega_{\mathrm{y}} \\ \omega_{\mathrm{z}} \end{bmatrix} \tag{6}$$

where OF_{j_i} is the OF component in the coordinate j of the point p_i, V_{k} and ω_{k} are respectively the translational and rotational rates of the body in the coordinate k. In practice, the origin of the image coordinate frame is not always at the principal point and the scaling for each image axis is different. Therefore, the image coordinates need an additional transformation matrix (K), which represents the intrinsic parameters of the camera. Finally, after calibration and considering the weak perspective projection we have:

$$\begin{aligned} x_i &= \frac{s_x f}{Z} X_i + x_0 \\ y_i &= \frac{s_y f}{Z} Y_i + y_0 \end{aligned} \tag{7}$$

where s_x and s_y are the scaling factors which take into account the pixel size, and (x_0, y_0) is the origin of the image coordinate system. This new transformation provides the true equations relating the OF with the 3D motion of the aircraft.

Once the object is detected (see Fig. 3), the visual system is able to sense the 6-DOF of the aircraft. However, we are only interested in translational velocities. Provided that the points and the vehicle share the same motion, then, we can express the mean of the OF as:

$$\begin{aligned} \frac{\sum OF_{x_i}}{n} &= \frac{\sum T_{OFx_i}}{n} + \frac{\sum R_{OFx_i}}{n} \\ \frac{\sum OF_{y_i}}{n} &= \frac{\sum T_{OFy_i}}{n} + \frac{\sum R_{OFy_i}}{n} \end{aligned} \tag{8}$$

with

$$\begin{aligned} \frac{\sum T_{OFx_i}}{n} &= -\frac{V_{\mathrm{x}}}{Z} - \frac{\sum x_i}{n}\frac{V_{\mathrm{z}}}{Z} \\ \frac{\sum R_{OFx_i}}{n} &= \frac{\sum x_i y_i}{n}\omega_{\mathrm{x}} - \frac{\sum\left(1 + x_i^2\right)}{n}\omega_{\mathrm{y}} + \frac{\sum y_i}{n}\omega_{\mathrm{z}} \\ \frac{\sum T_{OFy_i}}{n} &= -\frac{V_{\mathrm{y}}}{Z} - \frac{\sum y_i}{n}\frac{V_{\mathrm{z}}}{Z} \\ \frac{\sum R_{OFy_i}}{n} &= \frac{\sum\left(1 + y_i^2\right)}{n}\omega_{\mathrm{x}} - \frac{\sum x_i y_i}{n}\omega_{\mathrm{y}} - \frac{\sum x_i}{n}\omega_{\mathrm{z}} \end{aligned} \tag{9}$$

where n is the number of points having an OF estimation. It is assumed that a rich textured-features selector algorithm is used and that the search zone is on the vehicle's surface.

The average of the measured OF in the image coordinate system can be represented as

$$\begin{aligned}\dot{x} &= -\frac{V_x}{Z} - K_x^x\frac{V_z}{Z} + K_{xy}^x\omega_x - K_{x^2}^x\omega_y + K_y^x\omega_z \\ \dot{y} &= -\frac{V_y}{Z} - K_y^y\frac{V_z}{Z} + K_{y^2}^y\omega_x - K_{xy}^y\omega_y - K_x^y\omega_z\end{aligned} \tag{10}$$

where $\frac{V_x}{Z}$ and $\frac{V_y}{Z}$ are the relative velocities of the aircraft in the camera coordinate system, $\frac{V_z}{Z}$ is the inverse of the Time-To-Contact, known as the relative depth, and K_j^i is a constant scale factor depending on the intrinsic parameters of the camera. The rotations about the optical axis produce linear contributions to the OF, while both translation and rotation lead to non linear contributions. For rotations, the constant scale factor can be computed as a function of the intrinsic parameters of the camera and the output vectors of the rich textured-features detector. Once the scale factor is computed, the elimination of the rotational OF components is performed by the Kalman filter.

2.3 Kalman-based Sensor Fusion

The goal is to remove the ROF obtained during the motion of the vehicle. For this purpose inertial sensors are used in the estimation algorithm. The OF measurement involves uncertainties so that the TOF estimation problem can be set in the Kalman filter framework [13].

Given that the rotational components of the optical flow do not depend on the distance between the aircraft ant the camera, it is possible to use the vehicle state to estimate and compensate the contribution of the rotations. The remaining flow will be due to the translational velocity of the aircraft.

The following linear discrete-time state-space representation can be obtained from (2) and (10)

$$\begin{bmatrix} X \\ V \\ W \end{bmatrix}_k = \begin{bmatrix} I & T & 0 \\ 0 & I & 0 \\ 0 & 0 & I \end{bmatrix} \begin{bmatrix} X \\ V \\ W \end{bmatrix}_{k-1} + \begin{bmatrix} \upsilon_1 \\ \upsilon_2 \\ \upsilon_3 \end{bmatrix}_k \tag{11}$$

where X is the position, V is the velocity and W is the angular velocity of the vehicle. T represents the sampling period and υ_i represents the noise. The measured outputs are the computed barycenters X_V, the OF measurement V_{OF}, and the measured angular velocity W_{IMU}. The outputs are related to the state in (11) as

$$\begin{bmatrix} X_V \\ V_{OF} \\ W_{IMU} \end{bmatrix}_k = \begin{bmatrix} I & 0 & 0 \\ 0 & I & K_R^T \\ 0 & 0 & I \end{bmatrix} \begin{bmatrix} X \\ V \\ W \end{bmatrix}_k + \begin{bmatrix} \nu_1 \\ \nu_2 \\ \nu_3 \end{bmatrix}_k \tag{12}$$

where the noises in (11) and (12) are:

- $\upsilon = [\upsilon_1, \upsilon_2, \upsilon_3]^T$ is assumed to be a white noise with zero mean and known constant covariance matrix Q.
- $\nu = [\nu_1, \nu_2, \nu_3]^T$ is assumed to be a white noise with zero mean and known constant covariance matrix R.
- υ and ν are assumed to be uncorrelated noises.

The embedded Kalman filter implemented on the aircraft follows the correction-prediction sequence. The correction equation is the first step of the filter and given by

$$\begin{bmatrix} \hat{X} \\ \hat{V} \\ \hat{W} \end{bmatrix}_{k|k} = \begin{bmatrix} \hat{X} \\ \hat{V} \\ \hat{W} \end{bmatrix}_{k|k-1} + K \begin{bmatrix} X_V - \hat{X}_{k|k-1} \\ V_{OF} - \hat{V}_{k|k-1} - K_R^T \hat{W}_{k|k-1} \\ W_{IMU} - \hat{W}_{k|k-1} \end{bmatrix} \tag{13}$$

with

$$K = \begin{bmatrix} K_{x|x} & K_{x|v} & K_{x|i} \\ K_{v|x} & K_{v|v} & K_{v|i} \\ K_{i|x} & K_{i|v} & K_{i|i} \end{bmatrix} \tag{14}$$

The correction of the covariance matrix of the estimated error is computed as follows

$$P_{k|k} = (I - KC) P_{k|k-1} (I - KC)^T + KRK^T \tag{15}$$

with

$$(I - KC) = \begin{bmatrix} I - K_{x|x} & -K_{x|v} & -\left(K_R^T K_{x|v} + K_{x|i}\right) \\ -K_{v|x} & I - K_{v|v} & -\left(K_R^T K_{v|v} + K_{v|i}\right) \\ -K_{i|x} & -K_{i|v} & I - \left(K_R^T K_{i|v} + K_{i|i}\right) \end{bmatrix} \tag{16}$$

$$KRK^T = \begin{bmatrix} K_{x|x} R_x & K_{x|v} R_v & K_{x|i} R_i \\ K_{v|x} R_x & K_{v|v} R_v & K_{v|i} R_i \\ K_{i|x} R_x & K_{i|v} R_v & K_{i|i} R_i \end{bmatrix} \begin{bmatrix} K_{x|x}^T & K_{v|x}^T & K_{i|x}^T \\ K_{x|v}^T & K_{v|v}^T & K_{i|v}^T \\ K_{x|i}^T & K_{v|i}^T & K_{i|i}^T \end{bmatrix} \tag{17}$$

The prediction of the state is obtained from

$$\begin{bmatrix} \hat{X} \\ \hat{V} \\ \hat{W} \end{bmatrix}_{k+1|k} = \begin{bmatrix} I & T & 0 \\ 0 & I & 0 \\ 0 & 0 & I \end{bmatrix} \begin{bmatrix} \hat{X} \\ \hat{V} \\ \hat{W} \end{bmatrix}_{k|k} \tag{18}$$

The estimated error is predicted as follows.

$$P_{k+1|k} = \begin{bmatrix} I & T & 0 \\ 0 & I & 0 \\ 0 & 0 & I \end{bmatrix} P_{k|k} \begin{bmatrix} I & 0 & 0 \\ T^t & I & 0 \\ 0 & 0 & I \end{bmatrix} + \begin{bmatrix} Q_x & 0 & 0 \\ 0 & Q_v & 0 \\ 0 & 0 & Q_i \end{bmatrix} \tag{19}$$

with

$$P = \begin{bmatrix} P_{x|x} & P_{x|v} & P_{x|i} \\ P_{v|x} & P_{v|v} & P_{v|i} \\ P_{i|x} & P_{i|v} & P_{i|i} \end{bmatrix} \tag{20}$$

The Kalman gain is directly given by

$$K = P_{k+1|k} C^T \left(C P_{k+1|k} C^T + R \right)^{-1} \tag{21}$$

where

$$C P_{k+1|k} C^T = \begin{bmatrix} I & 0 & 0 \\ 0 & I & K_R^T \\ 0 & 0 & I \end{bmatrix} P_{k+1|k} \begin{bmatrix} I & 0 & 0 \\ 0 & I & 0 \\ 0 & \left(K_R^T\right)^T & I \end{bmatrix} \tag{22}$$

3 Dynamical Model

The vehicle used as proof-of-concept platform is mechanically simpler than classical helicopters, it does not have swashplate and has fixed-pitch blades (Figs. 4 and 5). The force f_i produced by motor i is proportional to the square of the angular speed, that is $f_i = k\omega_i^2$. The left and right motors rotate clockwise and counterclockwise respectively. Gyroscopic effects and aerodynamic torques tend to cancel in trimmed flight. The altitude relies on the vertical thrust, which is the sum of the forces provided by each motor. The rolling torque is obtained by differential motor thrust. The control surfaces are within the propellers airflow, which in combination with a deflection provides a torque. Thus the pitching torque depends on the elevator deflection (δ_e) while the yawing torque is produced by the differential deflection of the ailerons (δ_a) .

Let us denote $\mathcal{I} = \{i_i, j_i, k_i\}$ as the inertial frame, $\mathcal{B} = \{i_b, j_b, k_b\}$ as the body frame attached to the aircraft (Fig. 4) and $q_e = \left[x\ y\ z\ \phi\ \theta\ \psi\right]^T = [\xi\ \eta]^T$ as the generalized coordinates which describe the vehicle's position and attitude. $\xi \in \mathbb{R}^3$, denotes the position of the vehicle's center of gravity, relative to the inertial frame, and $\eta \in \mathbb{R}^3$ are the three Euler angles (roll, pitch and yaw), which represent the aircraft's orientation.

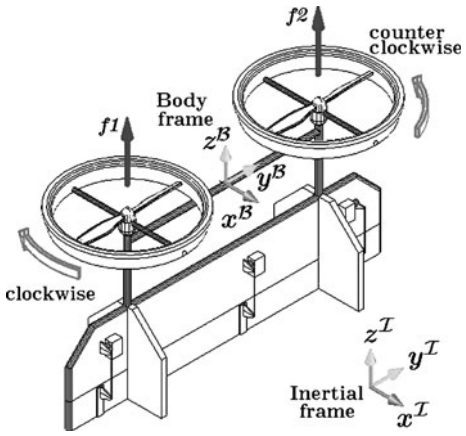

Fig. 4 Coordinates systems: inertial and body-fixed frames

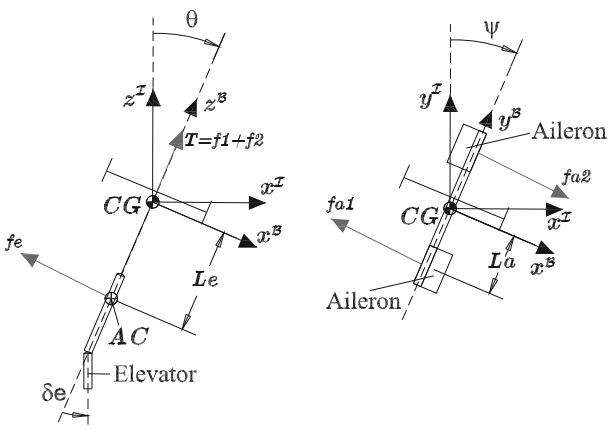

Fig. 5 Forces distribution in the vehicle

The dynamical model is obtained via the Euler-Lagrange formulation. The application of methodology results in the following equations of motion

$$m\ddot{\xi} + mG = \mathcal{R}^{\mathcal{BI}} F^{\mathcal{B}} \tag{23}$$

$$\mathbb{I}\ddot{\eta} + \dot{\mathbb{I}}\dot{\eta} - \frac{1}{2}\frac{\partial}{\partial \eta}\left(\dot{\eta}^T \mathbb{I}\dot{\eta}\right) = \tau^{\mathcal{B}} \tag{24}$$

where $m \in \mathbb{R}$ denotes the mass of the vehicle, $\tau \in \mathbb{R}^3$ denotes the generalized momentum, $F^{\mathcal{B}} \in \mathbb{R}^3$ is the force which affects the linear motion of the miniUAV, $G \in \mathbb{R}^3$ denotes gravity acceleration ($G = -g\, k_i$). The orthonormal transformation matrix $\mathcal{R}^{\mathcal{BI}}$ from the body frame to the inertial frame, with the rotation sequence $\psi \to \theta \to \phi$, is given as

$$\mathcal{R}^{\mathcal{BI}} = \begin{pmatrix} c_\theta c_\psi & -s_\psi c_\theta & s_\theta \\ s_\psi c_\phi + c_\psi s_\theta s_\phi & c_\psi c_\phi - s_\psi s_\theta s_\phi & -c_\theta s_\phi \\ s_\psi s_\phi + c_\psi c_\theta c_\phi & c_\psi s_\phi + s_\psi s_\theta c_\phi & c_\theta c_\phi \end{pmatrix} \tag{25}$$

where, for convenience, we denote $\sin(\cdot) \triangleq s_{(\cdot)}$ and $\cos(\cdot) \triangleq c_{(\cdot)}$. The term $\mathbb{I}$ is given by

$$\mathbb{I}(\eta) = \mathcal{W}^T I \mathcal{W} \tag{26}$$

where, $I \in \mathbb{R}^3$ describes the Inertia tensor matrix, which is diagonal due to the vehicle has two planes of symmetry. $\mathcal{W}$ is the non-orthonormal transformation that relates the angular velocity vector (Ω) and the Euler rate vector ($\dot{\eta}_2$)

$$\Omega = \mathcal{W}\dot{\eta} = \begin{pmatrix} C_\theta C_\psi & -S_\psi & 0 \\ C_\theta S_\psi & C_\psi & 0 \\ S_\theta & 0 & 1 \end{pmatrix} \begin{pmatrix} \dot{\phi} \\ \dot{\theta} \\ \dot{\psi} \end{pmatrix}. \tag{27}$$

Let us define the Coriolis and gyroscopic terms as

$$C(\eta, \dot{\eta})\,\dot{\eta} \triangleq \dot{\mathbb{I}}\dot{\eta} - \frac{1}{2}\frac{\partial}{\partial \eta}\left(\dot{\eta}^T \mathbb{I}\dot{\eta}\right) \tag{28}$$

Then, the rotational model (24) can be written as

$$\mathbb{I}\ddot{\eta} = \tau^{\mathcal{B}} - C(\eta, \dot{\eta}) \tag{29}$$

where, $\tau^{\mathcal{B}}$ represent the torque produced by the actuators

$$\tau_\phi = (f_1 - f_2) L_a \tag{30}$$

$$\tau_\theta = f_e L_e \tag{31}$$

$$\tau_\psi = (f_{a_1} + f_{a_1}) L_a \tag{32}$$

where l_m is the distance from each motor to the center of gravity (CG) while l_e and l_a are the distances from the CG to the aerodynamic center of each control surface.

The scalar equations corresponding to the translational dynamic model (23) are

$$\begin{cases} \ddot{x} = \dfrac{1}{m} T s_\theta \\ \ddot{y} = -\dfrac{1}{m} T c_\theta s_\phi \\ \ddot{z} = \dfrac{1}{m} T c_\theta c_\phi - g \end{cases} \tag{33}$$

with $T = f_1 + f_2$. For further control analysis, the following change of input variables is considered

$$\tau^{\mathcal{B}} = \mathbb{I}\tilde{\tau} + C(\eta, \dot{\eta}) \tag{34}$$

with $\tilde{\tau} = (\tilde{\tau}_\phi, \tilde{\tau}_\theta, \tilde{\tau}_\psi)^T$. Therefore, the rotational dynamical model (29) is written as

$$\begin{cases} \ddot{\phi} = \tau_\phi \\ \ddot{\theta} = \tau_\theta \\ \ddot{\psi} = \tau_\psi \end{cases} \tag{35}$$

4 Control Strategy

The vehicle's position is computed from two cameras as discussed previously (see Fig. 1). The frontal camera (cam_y) provides the feedback to control the altitude z and the $y - \phi$ underactuated subsystem, while, the lateral camera (cam_x) is devoted to the $x - \theta$ underactuated system. Thus, the dynamic system (33–35) can be split into the three following subsystems:

$$S_{cam_y} : \begin{cases} \ddot{y} = -\dfrac{1}{m} F_T \sin\phi \\ \ddot{\phi} = \tilde{\tau}_\phi \\ \ddot{z} = \dfrac{1}{m} F_T \cos\phi - g \end{cases} \tag{36}$$

$$S_{cam_x} : \begin{cases} \ddot{x} = \dfrac{1}{m} F_T \sin\theta \\ \ddot{\theta} = \tilde{\tau}_\theta \end{cases} \tag{37}$$

$$S_\psi : \{ \ddot{\psi} = \tilde{\tau}_\psi \tag{38}$$

For simplicity in the control analysis we consider the normalized values of the mass m, and the inertia moments matrix I (I_x,I_y,I_z).

4.1 Frontal Subsystem (S_{cam_y})

The control algorithm used for the frontal dynamic subsystem S_{cam_y}, focuses on the altitude followed by the $y-\phi$ stabilization. The altitude can be stabilized with a feedback-linearizable input via the thrust F_T. A suitable choice is

$$F_T = \frac{v_z + g}{\cos(\phi)} \tag{39}$$

where, $v_z = -a_{z_1}\dot{z} - a_{z_2}(z - z^d)$ with $a_{z_1}, a_{z_2} > 0$ and z_d is the desired altitude. From (39) we notice that the controller is valid within $-\frac{\pi}{2} < \phi < \frac{\pi}{2}$, which is appropriate for our flight purposes. Using (39) in (36) leads to

$$\ddot{y} = -\tan\phi\big(v_z + g\big) \tag{40}$$

Given that the flight of the aircraft evolves close to the vertical, we are able to consider $\tan\phi \approx \phi$. Also, note that $z \to z^d$ and therefore $v_z \to 0$. As a result the subsystem $(y-\phi)$ can be rewritten as

$$\begin{aligned} \ddot{y} &= -g\phi \\ \ddot{\phi} &= \tilde{\tau}_\phi \end{aligned} \tag{41}$$

which is a system composed of four integrators in cascade. To stabilize such system, we have used the following saturation-based control (for details see [14])

$$\tilde{\tau}_\phi = -\sigma_a\big(z_1\big) - \sigma_b\big(z_2\big) - \sigma_c\big(z_3\big) - \sigma_d\big(z_4\big) \tag{42}$$

where $z_1 = \dot{\phi}$, $z_2 = z_1 + \phi$, $z_3 = z_2 + \phi + \dot{y}$, $z_4 = z_3 + \phi + 2\dot{y} + y$ and σ_η is a saturation function defined as

$$\sigma_\eta(s) = \begin{cases} \eta & s > \eta \\ s & -\eta \le s \le \eta \\ -\eta & s < -\eta \end{cases} \tag{43}$$

4.2 Lateral Subsystem (S_{cam_x})

Assuming that the attitude is close to the origin and that the altitude has reached the desired value, the subsystem (37) can be rewritten as

$$\begin{aligned} \ddot{x} &= -g\theta \\ \ddot{\theta} &= \tau_\theta \end{aligned} \tag{44}$$

The same control algorithm is employed to stabilize (44), which is

$$\tau_\theta = -\sigma_a\big(z_1\big) - \sigma_b\big(z_2\big) - \sigma_c\big(z_3\big) - \sigma_d\big(z_4\big) \tag{45}$$

where $z_1 = \dot{\theta}$, $z_2 = z_1 + \theta$, $z_3 = z_2 + \theta + \dot{x}$, $z_4 = z_3 + \theta + 2\dot{x} + x$.

4.3 Heading Subsystem (S_ψ)

The yaw dynamics is described by the linear double integrator equation: $\ddot{\psi} = \tau_\psi$, and whose stabilization can be obtained using the following control input

$$\tilde{\tau}_\psi = -a_{\psi_1}\dot{\psi} - a_{\psi_2}(\psi) \tag{46}$$

with $a_{\psi_1}, a_{\psi_2} > 0$.

5 Experimental Testbed and Results

The goal of the experiment is to achieve an autonomous stabilized flight in attitude and position for a two-rotor VTOL (Vertical Take-Off and Landing) mini UAV. The visual algorithm provides the position feedback while the embedded inertial system provides the attitude. The system is described next:

- VTOL prototype:
  The vehicle's fuselage is built of foam and carbon fiber. The UAV's propulsion relies on two brushless motors with two counter rotating blades, while, the control surfaces (elevator and ailerons) are controlled through analog servomotors.
- Onboard system
  - Microcotroller:
    A Rabbit 3400 manages the position and attitude feedback signals. It processes the control algorithm to send the PWM signals to the power interface. The RC-PPM (Pulse Position Modulated) signal from the radio, is captured and decoded so that the user can introduce an external input. Indeed, the position feedback is triggered by an external RC signal.
  - Inertial sensors:
    A Microstrain 3DM-GXI is employed to sense the attitude of the vehicle (angular rate and angular position).
- Outboard system:
  The visual system is implemented outboard on a PC. The vision algorithms provide the centroid detection (position) and optical flow (velocity), which are sent to the aircraft via modem Xbee at 38400 bauds.

Figure 6 shows the overall position and velocity estimation strategy.

5.1 Experimental Results

The systems was tested in real time flight. In the experiments the vision algorithm was running at 14 Hz, which is sufficient to achieve position stabilisation. Figures 7 and 8 show the performance of the visual system and the embedded control law. In Fig. 8, the reference frame is translated to the chosen point where the rotorcraft is stabilized.

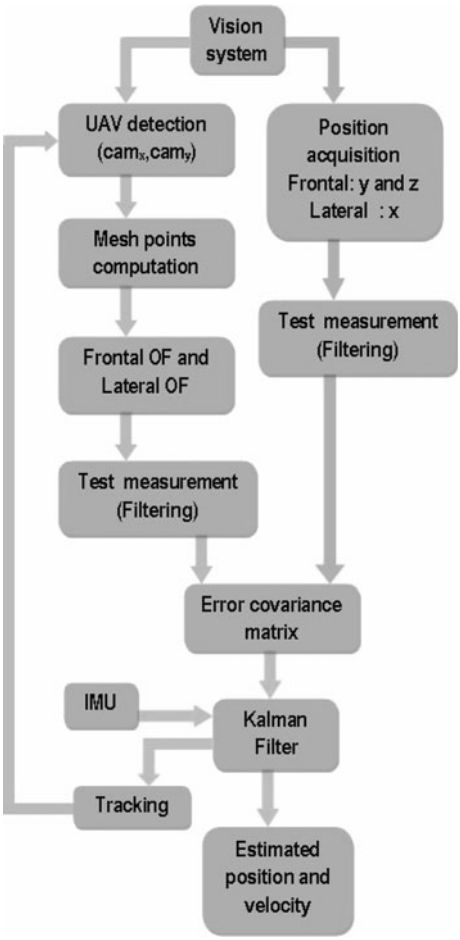

Fig. 6 Flow diagram of the position and velocity estimation

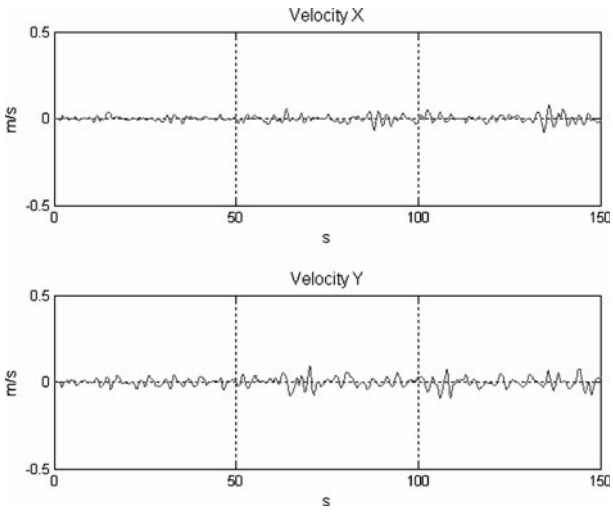

Fig. 7 Experimental results: velocity of the aircraft

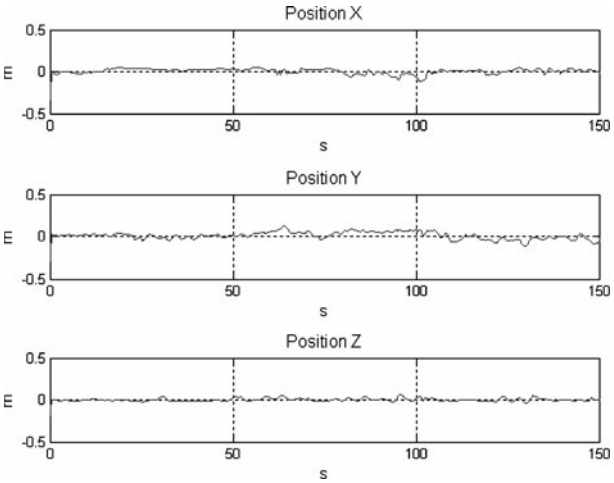

Fig. 8 Experimental results: position of the aircraft

6 Concluding Remarks

A strategy for autonomous hovering of a mini UAV has been presented using the combination of visual and inertial information. An embedded IMU has been used to obtain the orientation and angular velocity of the vehicle. The aircraft position has been computed using two external cameras arranged orthogonally to provide frontal and lateral views of the vehicle. The Viola-Jones object detection algorithm was used to compute the centroid of a pattern of points on the surface of the vehicle. This detection method is also promising for embedded applications (strapdown cameras) since the algorithm is tuned before the flight using image samples of the surrounding environment.

The position and velocity estimation problem has been set in the Kalman filter framework allowing the fusion of inertial measurements and visual information. A control strategy based on saturation functions has been proposed to stabilize the aircraft at hovering flight. The proposed methodology has been implement in a real platform composed of a two-rotor VTOL and two external cameras. The vehicle has performed a successful fully autonomous flight during the experiments. The experimental tests validated the proposed estimation algorithm based on the fusion of inertial and vision information as well as the embedded control law.

References

1. Barron, J., Fleet, D., Beauchemin, S.: Performance of optical flow techniques. Int. J. Comput. Vis. **12**(1), 43–77 (1994)
2. Ruffier, F., Franceschini, N.: Optical flow regulation: the key to aircraft automatic guidance. Robot. Auton. Syst., Elsevier **50**, 177–194 (2005)
3. Zufferey, J.C., Floreano, D.: Toward 30-gram autonomous indoor aircraft: vision-based obstacle avoidance and altitude control. In: IEEE International Conference on Robotics and Automation. Barcelona, Spain (2005)
4. Serres, J., Ruffier, F., Viollet, S., Franceschini, N.: Toward optical flow regulation for wall-following and centering behaviours. Int. J. Adv. Robot. Syst. **3**(2), 147–154 (2006)

5. Muratet, L., Doncieux, S., Brière, Y., Meyer, J.A.: A contribution to vision-based autonomous helicopter flight in urban environments. Robot. Auton. Syst. **50**(4), 195–209 (2005)
6. Romero, H., Salazar, S., Sanchez, A., Lozano, R.: A new configuration having eight rotors: dynamical model and real time control. In: IEEE International Conference on Decision and Control. New Orleans, USA (2007)
7. Bhanu, B., Roberts, B., Ming, J.: Inertial navigation sensor integrated motion analysis for obstacle detection. In: Proceedings of the IEEE International Conference on Robotics and Automation, pp. 954–959 (1990)
8. Mukai, T., Ohnishi, N.: The recovery of object shape and camera motion using a sensing system with a video camera and a gyro sensor. In: Internation Conference of Computer Vision, pp. 411–417. Kerkyra, Crece (1999)
9. Tian, T.Y., Tomasi, C., Heeger, D.J.: Comparison of approaches to egomotion computation. In: Computer Vision and Pattern Recognition, pp. 315–320 (1996)
10. Viola, P., Jones, M.: Rapid object detection using a boosted cascade of simple features. In: Computer Vision and Pattern Recognition, pp. 511–518 (2001)
11. Bouguet, J.Y.: Pyramidal implementation of the Lucas Kanade feature tracker. Technical report, Intel Corporation, Microprocessor Research Lab. (1999)
12. Waxman, A.M., Duncan, J.: Binocular image flows. In: Proceedings of Workshop on Motion: Representation and Analysis, pp. 31–38 (1986)
13. Kalman, R.: Contributions to the theory of optimal control. Bol. Soc. Mat. Mex. **5**(1), 102–119 (1960)
14. Lozano, R., Castillo, P., Dzul, A.: Stabilization of the PVTOL: real-time application to a mini-aircraft. Int. J. Control **77**(8), 735–740 (2004)